



Nano-precipitation leading to linear zero thermal expansion over a wide temperature range in Ti22Nb

Haoliang Wang^a, Daniel Kuok Zheng Lai^{a,d}, Juping Xu^{b,c}, Wen Yin^{b,c}, Chenghao Song^a, Yuliang Zhao^a, Yang Yang^e, Matthias Bönisch^{f,*}, Zhenzhong Sun^{a,*}

^a Neutron Scattering Technical Engineering Research Center, School of Mechanical Engineering, Dongguan University of Technology, Dongguan 523808, China

^b Institute of High Energy Physics, Chinese Academy of Sciences (CAS), Beijing 100049, China

^c Spallation Neutron Source Science Center, Dongguan 523803, China

^d Department of Mechanical, Materials and Manufacturing Engineering, Faculty of Science and Engineering, University of Nottingham Malaysia 43500, Malaysia

^e School of Electromechanical Engineering, Guangdong University of Technology, Guangzhou 510006, China

^f Department of Materials Engineering, KU Leuven, 3001, Belgium

ARTICLE INFO

Article history:

Received 2 August 2021

Revised 9 August 2021

Accepted 14 August 2021

Available online 21 August 2021

Keywords:

Titanium alloys

Orthorhombic martensite

Thermal expansion anisotropy

Texture

Dilatometry

ABSTRACT

Certain cold-worked martensitic Ti-alloys exhibit tunable linear thermal expansion along a specific sample direction. These intriguing properties are related to the anisotropic thermal expansion of the orthorhombic α'' martensite. However, the tailored expansion obtained in this way is limited to the single-phase martensitic temperature field, below the reverse transformation of martensite into austenite. Here, we demonstrate that the orthorhombic α''_{iso} formed by diffusion can also regulate the thermal expansion using a prototypical Ti22Nb alloy. More importantly, the temperature range in which the tailored linear thermal expansion occurs is enormously broadened relative to the cold-worked martensitic alloy. We clarify the formation path of nano-sized α''_{iso} during thermal cycling and resolve the crystallographic relationship with the parent phase. These findings provide new routes for designing low/negative thermal expansion Ti-alloys with large operating temperature ranges.

© 2021 Acta Materialia Inc. Published by Elsevier Ltd. All rights reserved.

Ti-alloys with tailored thermal expansion are of growing interest for potential applications in engineering components requiring high dimensional stability, such as optical lenses, space-based telescopes, and antennas [1–4]. Their unique properties originate from the giant anisotropic thermal expansion of β -stabilizer-rich α'' phase with an orthorhombic crystal structure, which exhibits negative thermal expansion (NTE) along $\langle 010 \rangle_{\alpha''}$ paired with positive thermal expansion (PTE) along $\langle 100 \rangle_{\alpha''}$ and $\langle 001 \rangle_{\alpha''}$ for sufficient contents of β -stabilizing elements [5–7]. Macroscopically, different linear coefficients of thermal expansion (CTEs) ranging from positive to negative can be obtained by tailoring the texture and volume fraction of α'' , among which linear zero thermal expansion (ZTE) is a balanced state of PTE and NTE [8]. Revealing the evolution of α'' and texture during thermomechanical treatments of β -stabilized Ti-alloys is essential for the successful technological application of their exceptional thermal expansion properties.

A previously demonstrated method for tailoring the CTE applies different levels of cold deformation on quenched Ti-alloys

containing either α'' martensite or metastable β phase [9,10]. Textures with the preferred $\langle 010 \rangle_{\alpha''}$ orientation can be introduced in quench-induced or stress-induced α'' martensite, leading to a low or negative CTE in specific sample directions [11]. In the case of rolling this direction is parallel to the rolling direction (RD). However, tailored thermal expansion obtained by cold working is limited to the temperature range below the austenite start (A_s) temperature. Above A_s the transformation strain due to the $\alpha'' \rightarrow \beta$ reversion alters the sample length remarkably [12]. Another approach is to impose heating on deformed samples that already have modified CTEs. Taking advantage of compositional fluctuations of the β -stabilizer, a transitory phase with the same orthorhombic structure as α'' martensite forms in a diffusion-controlled process upon heating [13]. Currently, there is no clear consensus in the literature on the naming of this orthorhombic phase, which has been reported in different β -stabilized Ti-alloys [14–19]. It was labeled α''_{iso} , O', and 'orthorhombic crystal' by different authors. Here, α''_{iso} will be used to refer to the diffusional, orthorhombic transition products formed before α precipitation. Previously it was demonstrated in Ti-24Nb-4Zr-8Sn [20] that the temperature range with stable, tailored thermal expansion is expanded to ~ 300 °C, much higher than A_s (~ 80 °C) of stress-

* Corresponding authors.

E-mail addresses: matthias.bonisch@kuleuven.be (M. Bönisch), sunzz@dgut.edu.cn (Z. Sun).

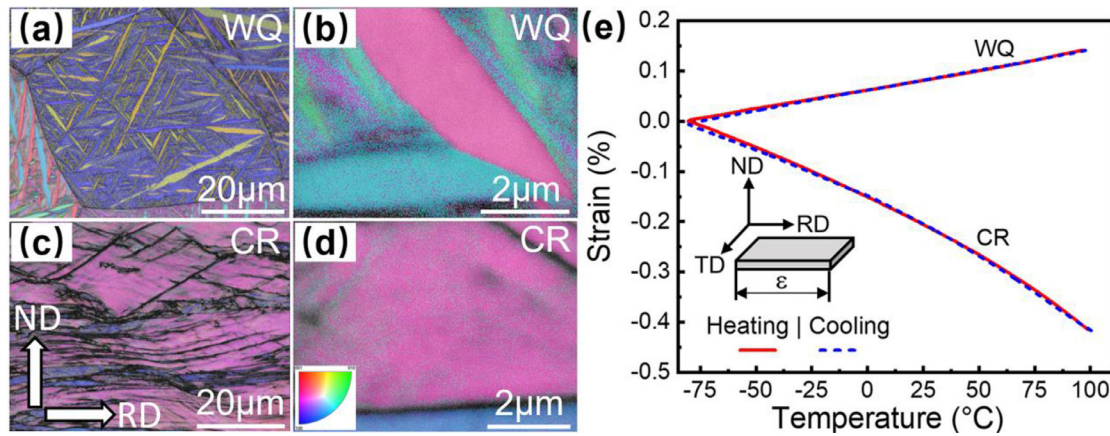


Fig. 1. EBSD band contrast (BC) maps overlaid with inverse pole figure (IPF) coloring of the microstructure of the Ti22Nb sheets in (a,b) water-quenched (WQ) and (c,d) cold-rolled (CR) conditions. (e) Single-cycle TMA measurements for the WQ and CR Ti22Nb sheets below the A_s temperature. The inset in (e) shows the measuring direction is along the rolling direction (RD).

induced α'' martensite. Yet to date, observations of the corresponding microstructure consisting of β -matrix, α''_{iso} , possibly ω and/or α , as well as an interpretation of the thermal expansion properties from the perspective of micro-texture are missing. To fully exploit the anisotropic thermal expansion of α''_{iso} , detailed microstructural investigations are necessary.

This study aims to unravel the phase transition sequences and their impact on the macroscopic CTE in a cold-rolled martensitic Ti22Nb (at.%). We employ neutron and X-ray diffraction to reveal the structural evolution associated with the transformation from initially linear NTE below A_s to linear ZTE in a broadened temperature range. Electron microscopy shows the nanoscale compositional, structural, and textural changes. An in-depth understanding of the orientation relationship between the α''_{iso} variants and the β matrix is crucial to explain the tailored CTEs. These results indicate that the volume fraction of α''_{iso} and the strength of the crystallographic texture are two important variables for developing Ti-alloys with bespoke thermal expansion.

A Ti22Nb ingot was produced by arc-melting high purity (99.99%) elemental Ti and Nb under Ar for 6 times. The ingot was homogenized at 1000 °C for 24 h in Ar and hot-rolled to a 10 mm thick plate at 850 °C in air. The plate was cut into sheets and cold-rolled down to 2 mm followed by annealing at 900 °C for 30 min in Ar-filled quartz tubes, water-quenching, and cold-rolling to 1 mm thickness. Conditions before and after the final cold-rolling will be referred to as the water-quenched (WQ) and cold-rolled (CR) states. The Nb and O content in both the WQ and CR sheets are 21.70 at.% and 0.42 at.%, measured by inductively coupled plasma optical emission spectroscopy and fusion-thermal conductivity method, respectively.

Scanning electron microscopy (SEM), electron backscatter diffraction (EBSD), and transmission Kikuchi diffraction (TKD) were conducted on a Carl Zeiss Gemini 300 microscope equipped with an Oxford Symmetry S2 EBSD detector and an Ultim Max energy dispersive X-ray spectroscopy (EDS) detector. Thermal expansion measurements were carried out at 3 °C/min with a Mettler Toledo TMA/SDTA841^e thermal mechanical analyzer (TMA) using rectangular samples ($8 \times 3 \times 1$ mm³). In-situ X-ray diffraction (XRD) was performed on a Rigaku Smartlab 9KW diffractometer equipped with a non-ambient stage and a MoK α target at a scan speed of 6°/min and a temperature change rate of 3 °C/min. Neutron diffraction (ND) was performed on the Multi-Physics Instrument at the China Spallation Neutron Source (CSNS) [21]. Eight rectangular sheets ($30 \times 8 \times 6$ mm³) were stacked to increase the gauge vol-

ume. Each pattern was collected for 2 h, while the sample rotated along the vertical axis with 3 °/s.

Fig. 1(a) and (c) show EBSD maps of WQ and CR samples respectively, viewed along the sheet transverse direction. The WQ sample has an equiaxed prior β grain structure with an average size of ~ 50 μ m, in which fine laths of α'' martensite are self-accommodated. The CR sample has a compressed grain structure. The enlarged micrographs of the martensite laths for WQ (Fig. 1(b)) and CR (Fig. 1(d)) samples show that none of ω and α phases exist inside the martensite laths. Fig. 1(e) shows the thermal expansion of WQ and CR samples along RD between -80 °C to 100 °C. In this temperature range, the α'' martensite maintains its orthorhombic structure, as the A_s temperature in Ti22Nb is ~ 150 °C [22]. The WQ sample exhibits linear PTE with a CTE of 8.81×10^{-6} , whereas the CR sample exhibits weak non-linear NTE with an average CTE of -20.35×10^{-6} . These results corroborate earlier studies [6,8,9] that the linear CTE of martensitic TiNb is easily adjusted by cold deformation.

To study the influence of heating into the temperature region of the reverse $\alpha'' \rightarrow \beta$ martensitic transformation (MT) and possible diffusional transformations, the CR sample was subjected to incremental heating from 0 °C, with the maximum temperature increased from 150 °C to 350 °C in steps of 100 °C. In the first cycle, the heating and cooling segments almost overlay, with only $\sim 0.02\%$ contraction at the end. In the second cycle, the sample contraction accelerates above ~ 150 °C, the thermal strain vs. temperature curve becomes distinctly nonlinear and the average CTE changes from -32.4×10^{-6} (0 °C–150 °C) to -102.1×10^{-6} (150 °C–250 °C). However, the large NTE is not stable. During cooling, the CTE changes to -38.2×10^{-6} (250 °C–150 °C) and further changes to -25.2×10^{-6} (150 °C to 0 °C). At the end of the second cycle, a contraction of 0.75% is present, evidencing the occurrence of microstructural changes (phase transformations, grain growth) in addition to thermal expansion. In the third cycle, the sample continues to contract above 250 °C and reaches its minimum length at ~ 300 °C. Afterward, the sample exhibits a positive CTE (300 °C–350 °C) but regains a negative CTE (350 °C–300 °C). The final contraction of the sample is 1.59%. The striking finding is that (quasi-)ZTE (CTE = -0.9×10^{-6}) is obtained during cooling from 300 °C to 0 °C. The thermal stability of the ZTE was examined using a fresh CR sample. As demonstrated in Fig. 2(b), ZTE between 0 °C and 300 °C is easily reproduced by heating to 350 °C and holding at 350 °C for 10 min. The ZTE behavior shows very good stability. During 7 cycles between 0 °C and 300 °C, the CTE changes only minimally (from 0.2×10^{-6} to 1.2×10^{-6}).

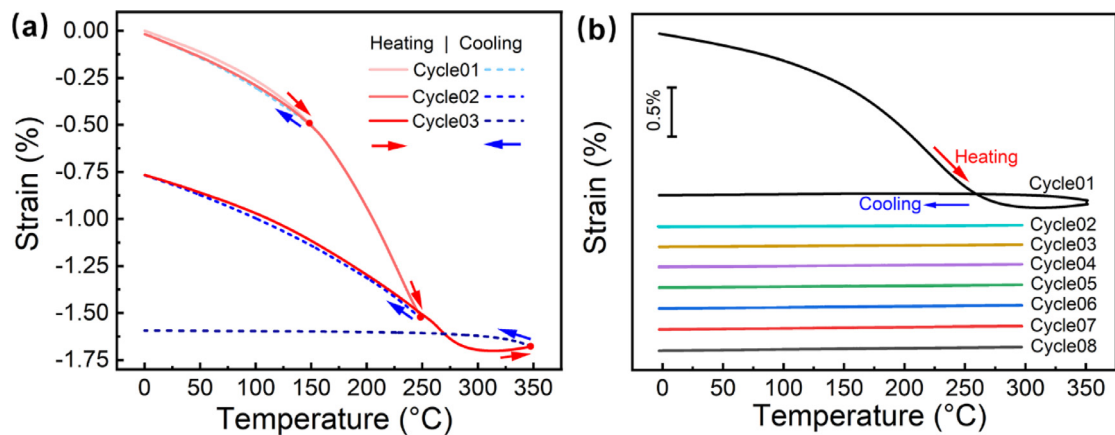


Fig. 2. TMA measurements for the Ti22Nb CR sheet along the rolling direction in (a) three thermal cycles with increasing maximum temperature (T_{max}) and (b) eight thermal cycles with $T_{max}=350^{\circ}\text{C}$ in cycle01 and $T_{max}=300^{\circ}\text{C}$ in cycle02–08.

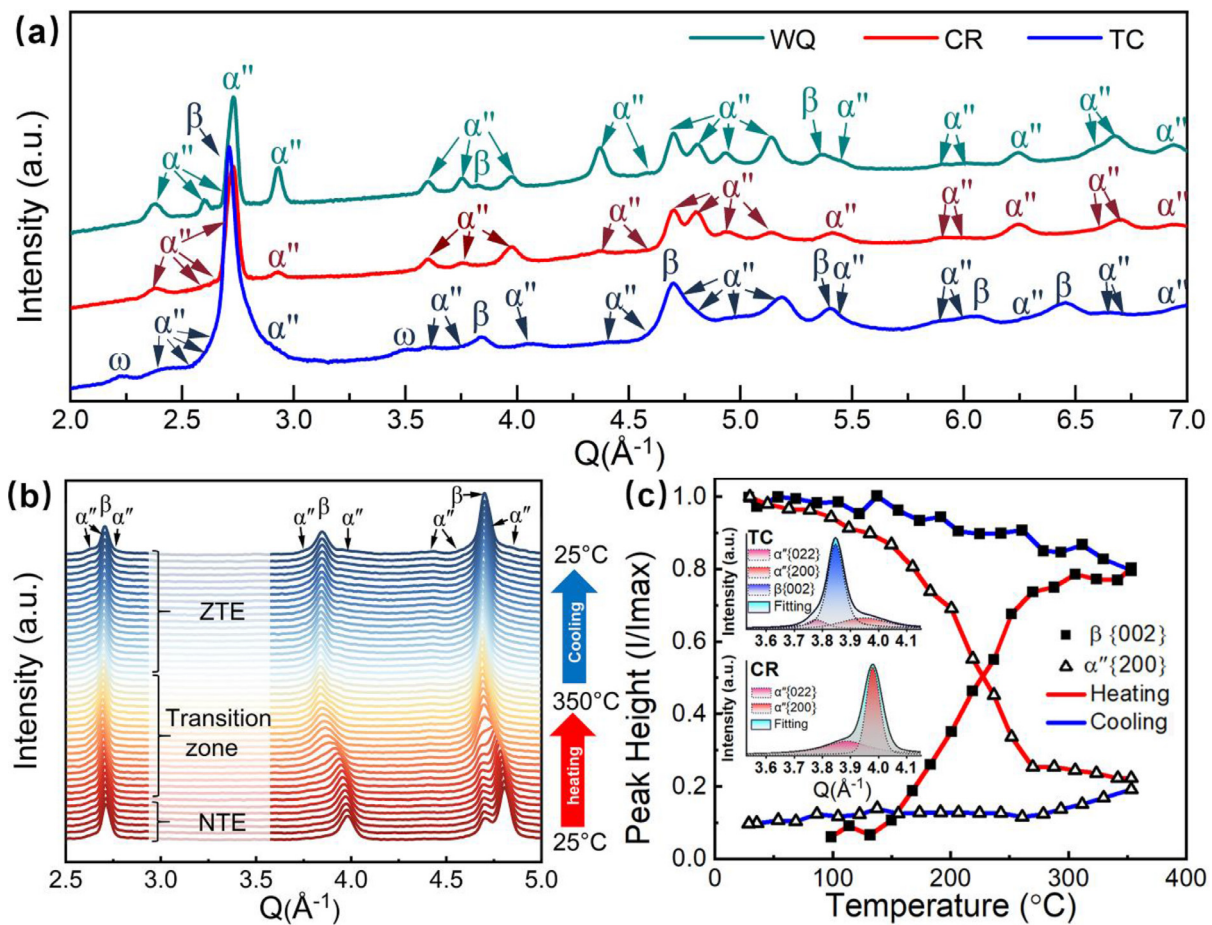


Fig. 3. (a) Neutron diffraction patterns of the water-quenched (WQ), cold-rolled (CR), and thermally-cycled (TC) Ti22Nb. (b) *In-situ* XRD patterns of the Ti22Nb CR sample in a thermal cycle between 25°C and 350°C . (c) Temperature dependence of the peak height of $\{002\}_{\beta}$ and $\{200\}_{\alpha'}$ normalized by dividing the maximum intensity of $\{002\}_{\beta}$ and $\{200\}_{\alpha'}$, respectively. The insets show the Rietveld refinements corresponding to the initial CR and final TC states.

To reveal the mechanisms for the conversion from NTE in CR sample to ZTE in thermally-cycled (TC) sample, the phase constitutions of Ti22Nb in three states, namely WQ, CR, and TC, were determined by ND at room temperature. The patterns in Fig. 3(a) show that the WQ and CR samples mainly consist of α'' martensite, with major differences in peak intensity and width owing to texture and strain broadening. A trace amount of β phase is found in the WQ sample, which is fully transformed to α'' martensite after cold rolling. The TC sample consists of β phase and minor amounts

of α'' and ω . Aiming to find the origin of ZTE, phase transformations in a CR sample during thermal cycling were characterized by *in-situ* XRD. Fig. 3(b) shows the stack of diffraction patterns with a temperature step of 15°C . Fig. 3(c) shows the evolution of the peak height of $\{002\}_{\beta}$ and $\{200\}_{\alpha'}$ normalized by dividing their respective maximum intensity. Two Rietveld refinements, corresponding to the initial CR and final TC states, are shown in the insets in Fig. 3(c). The whole cycle can be divided into three stages: (i) below $\sim 100^{\circ}\text{C}$, the peak height of α'' slightly decreases with rising

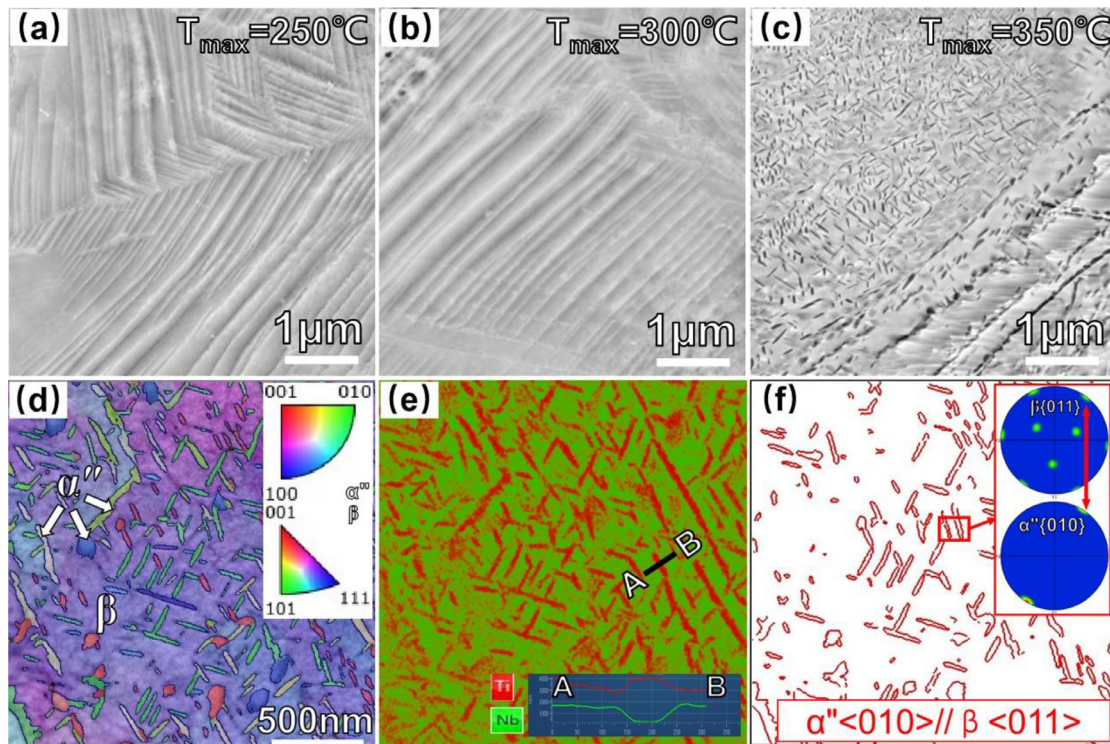


Fig. 4. SEM backscattered electron (BSE) image of Ti22Nb CR samples after heating to (a) 250 °C, (b) 300 °C, and (c) 350 °C. (d) TKD band contrast (BC) + inverse pole figure (IPF) map inside a primary α'' martensite lath in the same sample as in (c). (e) EDS map of Ti and Nb from the area shown in (d). The inset in (e) shows the element distribution along the line from A to B. (f) Highlighted β/α'' phase boundaries that obey the orientation relationship $\langle 010 \rangle_{\alpha''} // \langle 011 \rangle_{\beta}$. The insets in (f) show the pole figures of $\{011\}_{\beta}$ and $\{010\}_{\alpha''}$ planes from the area indicated by the red rectangle (For interpretation of the references to color in this figure legend, the reader is referred to the web version of this article.).

temperature. (ii) from ~ 100 °C to 350 °C and cooling from 350 °C to ~ 300 °C, β phase emerges and the reverse $\alpha'' \rightarrow \beta$ MT is evidenced by the drastic decrease and increase of α'' and β , respectively. Subsequently, the volume fraction of α'' and β change sluggishly between ~ 300 °C and 350 °C. (iii) from ~ 300 °C to 25 °C, the peak heights show little change with dropping temperature.

The *in-situ* XRD data and the TMA curve (cycle01 in Fig. 2(b)) yield the following conclusions. Firstly, the marked contraction starting from ~ 100 °C and ending at ~ 300 °C is the result of the $\alpha'' \rightarrow \beta$ MT. In more detail, rolling the WQ sheet induces a strong $\langle 010 \rangle_{\alpha''}$ texture along RD, as revealed by Monroe et al [6]. Kim et al investigated the lattice constants of β and α'' phases and found that the transformation strain of $\alpha'' \rightarrow \beta$ MT in the $\langle 010 \rangle_{\alpha''}$ direction is -4.2% [22]. As to the CR sample in which numerous $\{010\}_{\alpha''}$ planes are aligned perpendicular to RD [11], the contraction of the interplanar spacing could thus lead to macroscopic NTE, while the reverse MT is in progress. Secondly, given the coexistence of body-centered cubic (bcc) β and orthorhombic α'' and the absence of major changes in phase volume fractions (Fig. 3(c)), the ZTE is a composite effect of PTE in β and NTE in α'' . To fully understand the structure-property relationship prompting ZTE, the key question is whether α'' observed in the TC sample is (a) residual α'' martensite originally formed by quenching and remaining intact after CR and TC, or (b) α''_{iso} phase formed via diffusion.

As explained above, the contraction in CR sample during heating below 300 °C (TMA curves in Fig. 2) results from the reverse $\alpha'' \rightarrow \beta$ MT. However, the strain evolution above 300 °C remains to be explained, as the sample keeps on dilating during holding at 350 °C and cooling to 300 °C (cycle01 in Fig. 2(b)). Therefore, the microstructure of CR samples after heating to 250 °C, 300 °C, and 350 °C were further studied (Fig. 4(a–c)). Although the crystal structure changes, the lamellar morphology is preserved, af-

ter heating to 250 °C–300 °C (Fig. 4(a,b)). With 350 °C heating (Fig. 4(c)), fine precipitates dispersed in the matrix and along grain boundaries form. The ultimate phase composition inside a former primary α'' lath is revealed in Fig. 4(d), where TKD shows that the matrix is bcc and the precipitates are orthorhombic. The precipitates are present mostly as needles with a transverse diameter of 10–30 nm and a few elliptical particles of 40–100 nm. The EDS map in Fig. 4(e) evidences the exclusion of Nb accompanying the precipitation, i.e. the bcc matrix is Nb rich and the orthorhombic precipitates are Nb lean. The precipitates can thus be identified as α''_{iso} . Moreover, the α'' - β interfaces obeying the orientation relationship $\langle 010 \rangle_{\alpha''} // \langle 011 \rangle_{\beta}$ are presented in Fig. 4(f). The results indicate that most of the $\{010\}_{\alpha''}$ planes in the α''_{iso} phase are parallel to the $\{011\}_{\beta}$ planes in the β matrix.

The combined textural and structural analysis in Fig. 4 explains the thermal expansion above ~ 300 °C and the ZTE below ~ 300 °C as well as their connection to lattice thermal expansion. Beginning with a $\langle 010 \rangle_{\alpha''}$ texture along RD in the CR sample, the β phase inherits a $\langle 011 \rangle_{\beta}$ texture through the displacive MT during heating to ~ 300 °C, following the Au–Cd type lattice correspondence [23]. Above ~ 300 °C, the transitional α''_{iso} precipitates in a coupled diffusional-displacive transformation involving continuous chemical and structural changes towards equilibrium α phase [13]. Specifically, in the present work, α''_{iso} formed in β favors a $\langle 010 \rangle_{\alpha''}$ texture as revealed by TKD (Fig. 4(d)). The TC sample thus has a composite texture of $\langle 011 \rangle_{\beta}$ and $\langle 010 \rangle_{\alpha''}$ along RD. Crystallographically, the $\beta \rightarrow \alpha''$ transformation strain along $\langle 010 \rangle_{\alpha''}$ is positive ($\sim 4.2\%$ in Ti22Nb [22]). Additionally, β stabilizers significantly affect the lattice parameters of α'' , among which $b_{\alpha''}$ (interplanar spacing of $\{010\}_{\alpha''}$) is inversely proportional to the content of Nb, Mo, Ta [24–26]. As α''_{iso} rejects Nb into β , the increment in the transformation strain along $\langle 010 \rangle_{\alpha''}$ and the growth of α''_{iso}

contribute to the expansion along RD as long as the transformation sustains. During cooling below ~ 300 °C, the increased difficulty for Nb diffusion restrains the $\beta \rightarrow \alpha''_{\text{iso}}$ transformation and the intrinsic thermal expansion of β and α''_{iso} begins to dominate the length change. The expansion rates along $\langle 011 \rangle_{\beta}$ and $\langle 010 \rangle_{\alpha''}$ playing a central role were characterized previously [5]. It was shown that the CTE of $\{010\}_{\alpha''}$ in Ti(21–36)Nb (wt.%) (~ 12 – ~ 23 at.%) is negative and the CTE of $\{011\}_{\beta}$ in Ti36Nb (wt.%) (~ 23 at.%) is positive. In our alloy, Nb-lean α''_{iso} is considered to have a negative CTE along $\langle 010 \rangle_{\alpha''}$, while Nb-rich β has a positive CTE along $\langle 011 \rangle_{\beta}$. Therefore, the ZTE is due to a balance in phase composition and texture, with the negative strain of α''_{iso} opportunely offsetting the positive strain of β .

The slight increase of macroscopic CTE in Cycle02–08 in Fig. 2(b) also matches another feature of α'' mentioned earlier [5], namely that the ability of $\{010\}_{\alpha''}$ planes to contract upon heating increases with the Nb content. As the cumulative time during which the sample is exposed to a high temperature (near 300 °C) is extended, progressive depletion of Nb in α''_{iso} occurs. Consequently, the CTE of the whole sample increases due to the attenuated NTE of $\{010\}_{\alpha''}$ planes in α''_{iso} . Whether precipitation of α''_{iso} favors specific crystallographic variants rather than all variants with equal probability remains unclear at present. A further study focusing on the variant selection and manipulation of its texture is ongoing.

In summary, the present work testifies the feasibility of tailoring the linear CTE of pre-textured martensitic Ti22Nb by transitory heating through the diffusive transformation region above 300 °C. Consequently, transitional α''_{iso} forms through a diffusion-mediated pathway. The controllability of the linear CTE stems from the anisotropic thermal expansion of the orthorhombic lattice of α''_{iso} . As the nano-sized α''_{iso} precipitates form in the β matrix with a preferred orientation, lattice planes exhibiting negative CTE become aligned perpendicular to the rolling direction, thus critically influencing the macroscopic thermal expansion of the bulk sample.

Declaration of Competing Interest

The authors declare that they have no known competing financial interests or personal relationships that could have appeared to influence the work reported in this paper.

Acknowledgment

The work was financially supported by Project 51901042, 51801199, and U2032219 supported by NSFC, Project

2018KQNCX256 supported by Guangdong Province Office of Education, Project 2019A1515110467 supported by Guangdong Basic and Applied Basic Research Foundation, and Project TDQN2019005 supported by DGUT. We are grateful for the technical support from Oxford Instruments on TKD experiments.

References

- [1] Y. Wang, J. Gao, H. Wu, S. Yang, X. Ding, D. Wang, X. Ren, Y. Wang, X. Song, J. Gao, Sci. Rep. 4 (2014) 3995.
- [2] J.A. Monroe, J.S. McAllister, D.S. Content, J. Zgarba, X. Huerta, I. Karaman, Proc. SPIE 10706 (2018) 107060R.
- [3] J.A. Monroe, J.S. McAllister, D.S. Content, J. Zgarba, Proc. SPIE 11310 (2020) 1131013.
- [4] K.J. Loring, L.F. Ortega, J.A. Monroe, J.S. McAllister, X. Huerta, G. Mueller, P. Fulda, J. Astron. Telesc. Instrum. Syst. 6 (1) (2020) 015007.
- [5] M. Bönisch, A. Panigrahi, M. Stoica, M. Calin, E. Ahrens, M. Zehetbauer, W. Skrotzki, J. Eckert, Nat. Commun. 8 (1) (2017) 1429.
- [6] J.A. Monroe, D. Gehring, I. Karaman, R. Arroyave, D.W. Brown, B. Clausen, Acta Mater. 102 (2016) 333–341.
- [7] S. Demakov, I. Semkina, S.I. Stepanov, Mater. Sci. Forum 907 (2017) 14–20.
- [8] M. Bönisch, M. Stoica, M. Calin, Sci. Rep. 10 (2020) 3045.
- [9] D. Gehring, J.A. Monroe, I. Karaman, Scripta Mater. 178 (2020) 351–355.
- [10] S.I. Demakov, S.I. Stepanov, A.G. Illarionov, M.A. Ryzhkov, Phys. Met. Metallogr. 118 (3) (2017) 264–271.
- [11] D. Gehring, R. Yang, Z. Barghouti, I. Karaman, Acta Mater. 1 (2021) 116847.
- [12] M.A.-H. Gepreel, M. Niinomi, M. Nakai, M. Morinaga, JOM 71 (10) (2019) 3631–3639.
- [13] L. Qi, S. He, C. Chen, B. Jiang, Y. Hao, H. Ye, R. Yang, K. Du, Acta Mater. 195 (2020) 151–162.
- [14] E. Aeby-Gautier, A. Settefrati, F. Bruneseaux, B. Appolaire, B. Denand, M. Dehmas, G. Geandier, P. Boulet, J. Alloy. Compd. 577 (2013) S439–S443.
- [15] P. Barriobero-Vila, G. Requena, F. Warchomicka, A. Stark, N. Schell, T. Buslaps, J. Mater. Sci. 50 (3) (2015) 1412–1426.
- [16] M. Tahara, K. Hasunuma, H. Hosoda, J. Alloy. Compd. 868 (2021) 159237.
- [17] Y. Zheng, D. Banerjee, H.L. Fraser, Scripta Mater. 116 (2016) 131–134.
- [18] T. Li, M. Lai, A. Kostka, S. Salomon, S. Zhang, C. Somsen, M.S. Dargusch, D. Kent, Scripta Mater. 170 (2019) 183–188.
- [19] D.L. Gong, H.L. Wang, E.G. Obbard, S.J. Li, R. Yang, Y.L. Hao, J. Mater. Sci. Technol. 80 (2021) 234–243.
- [20] Y.L. Hao, H.L. Wang, T. Li, J.M. Cairney, A.V. Ceguerra, Y.D. Wang, Y. Wang, D. Wang, E.G. Obbard, S.J. Li, R. Yang, J. Mater. Sci. Technol. 32 (8) (2016) 705–709.
- [21] J. Xu, Y. Xia, Z. Li, H. Chen, X. Wang, Z. Sun, W. Yin, Nucl. Instrum. Methods Phys. Res. Sect. A 1013 (2021) 165642.
- [22] H.Y. Kim, Y. Ikehara, J.I. Kim, H. Hosoda, S. Miyazaki, Acta Mater. 54 (9) (2006) 2419–2429.
- [23] T. Inamura, H. Hosoda, H. Young Kim, S. Miyazaki, Philos. Mag. 90 (25) (2010) 3475–3498.
- [24] M. Bönisch, M. Calin, L. Giebler, A. Helth, A. Gebert, W. Skrotzki, J. Eckert, J. Appl. Crystallogr. 47 (2014) 1374–1379.
- [25] R. Davis, H.M. Flower, D. West, J. Mater. Sci. 14 (3) (1979) 712–722.
- [26] A.V. Dobromyslov, G.V. Dolgikh, Y. Dutkevich, T.L. Trenogina, Phys. Met. Metallogr. 107 (5) (2009) 502–510.